

The real-space clustering of luminous red galaxies around $z < 0.6$ quasars in the Sloan Digital Sky Survey

Nikhil Padmanabhan,¹[★]† Martin White,² Peder Norberg³ and Cristiano Porciani⁴

¹Physics Division, Lawrence Berkeley National Laboratory, 1 Cyclotron Rd., Berkeley, CA 94720, USA

²Department of Physics and Astronomy, 601 Campbell Hall, University of California Berkeley, CA 94720, USA

³The Scottish Universities Physics Alliance, Institute for Astronomy, University of Edinburgh, Royal Observatory, Blackford Hill, Edinburgh EH9 3HJ

⁴Institute for Astronomy, ETH Zurich, 8093 Zurich, Switzerland

Accepted 2008 October 9. Received 2008 September 29; in original form 2008 February 19

ABSTRACT

We measure the clustering of a sample of photometrically selected luminous red galaxies (LRGs) around a low-redshift ($0.2 < z < 0.6$) sample of quasars selected from the Sloan Digital Sky Survey Data Release 5. We make use of a new statistical estimator to obtain precise measurements of the LRG autocorrelations and constrain halo occupation distributions for them. These are used to generate mock catalogues which aid in interpreting our quasar-LRG cross-correlation measurements. The cross-correlation is well described by a power law with slope 1.8 ± 0.1 and $r_0 = 6 \pm 0.5 h^{-1}$ Mpc, consistent with observed galaxy correlation functions. We find no evidence for ‘excess’ clustering on 0.1 Mpc scales and demonstrate that this is consistent with the results of Serber et al. and Strand, Brunner and Myers, when one accounts for several subtleties in the interpretation of their measurements. Combining the quasar-LRG cross-correlation with the LRG autocorrelations, we determine a large-scale quasar bias $b_{\text{QSO}} = 1.09 \pm 0.15$ at a median redshift of 0.43, with no observed redshift or luminosity evolution. This corresponds to a mean halo mass $\langle M \rangle \sim 10^{12} h^{-1} M_{\odot}$, Eddington ratios from 0.01 to 1 and lifetimes less than 10^7 yr. Using simple models of halo occupation, these correspond to a number density of quasar hosts greater than $10^{-3} h^3 \text{Mpc}^{-3}$ and stellar masses less than $10^{11} h^{-1} M_{\odot}$. The small-scale clustering signal can be interpreted with the aid of our mock LRG catalogues, and depends on the manner in which quasars inhabit haloes. We find that our small-scale measurements are inconsistent with quasar positions being randomly subsampled from halo centres above a mass threshold, requiring a satellite fraction > 25 per cent.

Key words: galaxies: elliptical and lenticular, cD – quasars: general – large-scale structure of Universe.

1 INTRODUCTION

Quasars are among the most luminous astrophysical objects, and are believed to be powered by accretion on to supermassive black holes (e.g. Salpeter 1964; Lynden-Bell 1969). They have become a key element in our current paradigm of galaxy evolution – essentially, all spheroidal systems at present harbour massive black holes (Kormendy & Richstone 1995), the masses of which are correlated with many properties of their host systems. However, the physical mechanisms that trigger and fuel quasars are still unknown; furthermore, it is possible that very different mechanisms dominate at low and high redshifts and at high and low luminosities.

Deep imaging with the *Hubble Space Telescope* (HST) (e.g. Bahcall et al. 1997; McLure et al. 1999; Dunlop et al. 2003;

Floyd et al. 2004; Letawe et al. 2008) suggests that low- z quasi-stellar objects (QSOs) are exclusively hosted by bright galaxies with $L > L_*$. Radio-loud QSOs reside in early-type galaxies, while their radio-quiet counterparts have both early- and late-type hosts, with the fraction of early-type hosts increasing with the quasar optical luminosity. In most cases, there is strong observational evidence for the presence of a young (subdominant) stellar population (Sánchez et al. 2004) and large amounts of gas, irrespective of the morphological type of the host (Letawe et al. 2007). Furthermore, 30–50 per cent of quasars appear to be associated with interactions, although the number of such imaged systems is small, and signatures of mergers are notoriously difficult to observe. The emerging picture is that the QSO activity and star formation are inextricably linked (e.g. Nandra et al. 2007; Silverman et al. 2008) in galaxies that contain a massive bulge (and thus a massive black hole) and a gas reservoir.

The clustering of quasars as a function of redshift and luminosity provides a different perspective on the above picture. The amplitude

[★]E-mail: NPadmanabhan@lbl.gov

†Hubble Fellow, Chamberlain Fellow.

of clustering on large scales is related to the masses of the dark matter haloes which host the quasars (their environment), which together with the observed number density allows us to constrain the quasar lifetimes or duty cycles. The small-scale clustering of quasars can shed light on the triggering mechanism for quasars, and the nature of quasar progenitors.

However, it is only recently that samples of quasars have grown big enough (in terms of the number of objects) to study their clustering with some precision (Porciani, Magliocchetti & Norberg 2004; Croom et al. 2005; Hennawi et al. 2006; Porciani & Norberg 2006; Myers et al. 2007a,b; Shen et al. 2007; da Angela et al. 2008). One of the major problems with measuring the clustering of quasars is that they are extremely rare ($\bar{n} \sim 10^{-6} h^3 \text{Mpc}^{-3}$ at $z \sim 0.5$). Shot-noise from Poisson fluctuations in the counts of objects thus obscures their clustering signal. At low redshifts, this problem is exacerbated, requiring measurements in very broad redshift intervals.

To avoid this, we cross-correlate approximately 2500 low- z quasars (Schneider et al. 2007) with a sample of 450 000 luminous red galaxies (LRGs) (Padmanabhan et al. 2007), both selected from the Sloan Digital Sky Survey (SDSS, York et al. 2000) and with overlapping redshift distributions. The LRGs have very reliable photometric redshifts (Padmanabhan et al. 2005), trace the matter distribution in a way that is well understood and have a much higher volume density ($\bar{n} \sim 10^{-4} h^3 \text{Mpc}^{-3}$) than the quasar sample. The cross-correlation can thus be well measured and inverted, using the known redshift distribution, to the underlying 3D clustering.

In this paper, we make use of several novel techniques for measuring the clustering of galaxies and quasars, and compute full covariance matrices for our estimators from the data themselves. While the idea of enhancing the clustering signal by using cross-correlations is not new (Coil et al. 2007; Croom et al. 2004; Adelberger & Steidel 2005a,b; Serber et al. 2006; Strand et al. 2008; Mountrichas et al. 2009), the sample size and ability to perform such detailed statistical analyses are new to this paper. In addition, the precise measurements of LRG clustering allow us for the first time to discuss the manner in which both LRGs and quasars inhabit dark matter haloes at $z \sim 0.5$.

The outline of the paper is as follows. In Section 2, we describe the LRG and quasar samples, drawn from the SDSS, that we use. The clustering measurements are described in Section 3, where we pay special attention to the techniques used and the error estimates. The implications of our results for quasars are explored in Section 4, including comparisons with earlier work. In particular, we investigate the manner in which quasars inhabit dark matter haloes at $z \sim 0.5$. We conclude in Section 5. Appendix A contains the technical details of the halo model fits used in this paper, while Appendix B recasts the measurements of Serber et al. (2006) and Strand et al. (2008) into the framework of this paper, highlighting unappreciated subtleties in their interpretation. Where necessary we will assume a Λ cold dark matter (Λ CDM) cosmological model with $\Omega_{\text{mat}} = 0.25$, $\Omega_{\Lambda} = 0.75$ and $\sigma_8 = 0.8$. Also, unless the h dependence is explicitly specified, we assume $h = 0.7$.

2 DATA

2.1 Quasars

We use quasars selected from the fourth edition of the SDSS quasar catalogue (Schneider et al. 2007). This catalogue consists of spectroscopically identified quasars in the fifth SDSS data release (Adelman-McCarthy et al. 2007), with an absolute point spread

function (PSF) magnitude in the i band, $M_i < -22.0$ and at least one emission line with full width at half-maximum larger than 1000 km s^{-1} . It does not contain Type 2 QSOs, Seyferts or BL Lac objects. In order to construct a homogeneous sample, we follow Richards et al. (2006) and select objects

- (i) that were targeted for science (SCIENCEPRIMARY = 1);
- (ii) classified by the SDSS photometric pipeline as primary (PRIMARY = 1);
- (iii) morphologically consistent with being point sources (MORPHOLOGY = 0).
- (iv) with dust and emission-line K -corrected i -band magnitudes, $i < 19.1$.

In order to cross-correlate with the LRG sample described below, we restrict ourselves to quasars that lie within the LRG angular mask, and with redshifts between $0.25 < z < 0.6$. The resulting sample (denoted ALL below) has 2476 quasars. One subtlety with the SDSS quasar samples is the changes to the quasar target selection algorithm (Richards et al. 2002) over the lifetime of the survey. However, these changes were made to optimize target selection at high redshifts, and have little effect on our sample. As we discuss below, restricting to quasars selected with the final version of the QSO target selection (v3.1.0) does not affect any of our results. We therefore do not make a cut based on the target selection algorithm. The redshift distribution is shown in Fig. 1, while the angular distribution is in Fig. 2.

Fig. 3 plots the conditional magnitude distribution of our sample. We assume a redshift evolution of $M_{*,i}$ (k -corrected to $z = 0$) given by

$$M_{*,i}(z) = M_{*,i,0} - 2.5 (k_1 z + k_2 z^2), \quad (1)$$

with $M_{*,i,0} = -21.678$, $k_1 = 1.39$ and $k_2 = -0.29$ (Richards et al. 2005), where we have converted from the SDSS g to i band with $M_g - M_i = 0.068$ (Richards et al. 2006). This defines a sample of quasars (denoted LSTAR) with $M_i < M_{*,i}$, yielding a sample with an approximately constant spatial number density over the

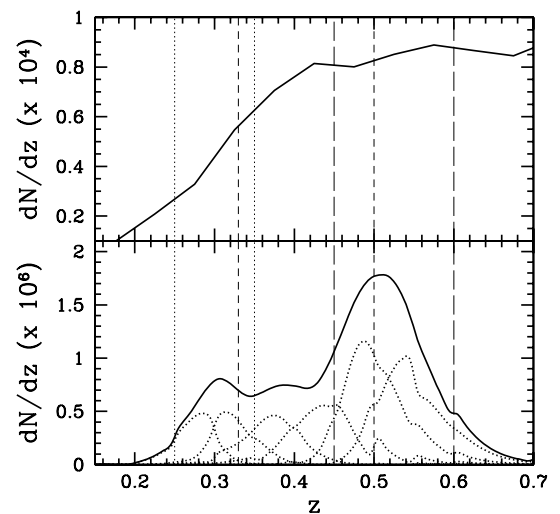


Figure 1. The redshift distribution of the quasars (top panel) and LRGs (bottom panel) used in this analysis. The LRG redshift distributions are derived from the observed photometric redshift distribution, after deconvolving the redshift errors. The dotted lines show the redshift distribution for the six individual $d z_{\text{photo}} = 0.05$ LRG samples. The vertical lines mark the boundaries of the three quasar redshift slices we consider $-0.25 < z < 0.35$ (dotted line), $0.33 < z < 0.50$ (short-dashed line) and $0.45 < z < 0.6$ (long-dashed line).

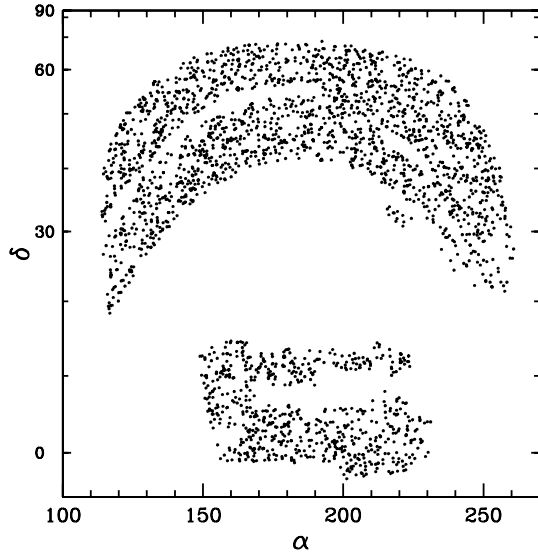


Figure 2. The angular distribution of our quasar sample, plotted in an RA-cos(δ) equal-area rectilinear projection. The angular mask for the quasars is determined both by the spectroscopic coverage and the overlap with the photometric LRG sample.

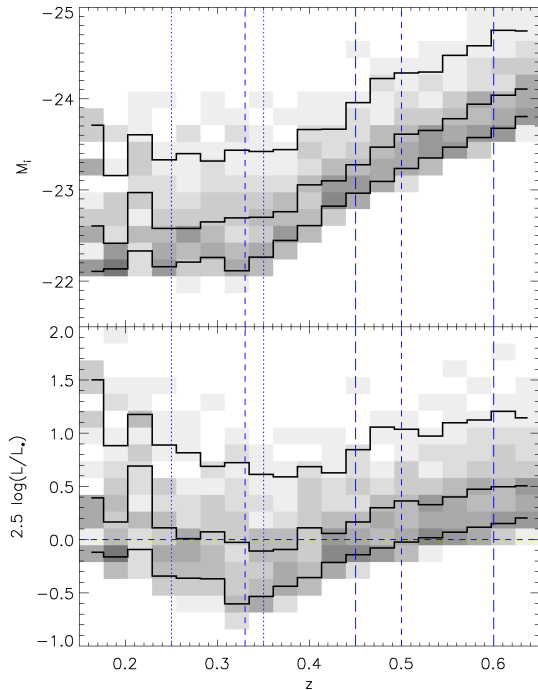


Figure 3. The conditional distribution of absolute magnitude with redshift for our sample of QSOs. The lines plot the 16, 50 and 84 per cent contours. The lower panel plots the absolute magnitude relative to M_* , estimated from the 2dF and 2SLAQ survey. The flattening/upturn at low redshift is due to the $M_i = -22.0$ cut on the sample, to minimize contamination from the host galaxy. The vertical lines (as in Fig. 1) show the redshift boundaries of our samples.

redshift range we consider. We can estimate the number density of these samples by integrating the broken power-law fit to the QSO luminosity function from Richards et al. (2005):

$$\Phi(L, z) = \frac{\Phi^*}{10^{0.4(\alpha+1)(M_i - M_{*,i})} + 10^{0.4(\beta+1)(M_i - M_{*,i})}}. \quad (2)$$

Table 1. A summary of the quasar we consider. The columns list the sample name, redshift range and the number of quasars.

Sample	Redshift	n_{QSO}
ALL0	$0.25 < z < 0.35$	435
ALL1	$0.33 < z < 0.50$	1277
ALL2	$0.45 < z < 0.60$	1269
LSTAR0	$0.25 < z < 0.35$	212
LSTAR1	$0.33 < z < 0.50$	751
LSTAR2	$0.45 < z < 0.60$	1094

If we assume the parameters estimated from the 2QZ and 2SLAQ surveys, i.e. $M_{*,i}$ as defined above, $\alpha = -3.31$, $\beta = -1.45$ and $\Phi^* = 5.33 \times 10^{-6} h^3 \text{Mpc}^{-3} \text{mag}^{-1}$ (Richards et al. 2005), and no scatter between g and i magnitudes, we estimate a number density of $1.7 \times 10^{-7} h^3 \text{Mpc}^{-3}$. If one adopts the parameters from Boyle et al. (2000), we find a number density of $\sim 1.3 \times 10^{-7} h^3 \text{Mpc}^{-3}$, approximately 20 per cent lower. Note that we keep the sample definition the same for both these cases, so one is integrating over magnitudes less than M_* defined by equation (1).

We estimate the bolometric luminosity using the relation from Croom et al. (2005):

$$M_i = -2.66 \log_{10}(L_{\text{bol}}) + 79.36, \quad (3)$$

where L_{bol} is in Watts (W), and we convert from the b_J to i band using the empirical relations in Richards et al. (2006). For the LSTAR sample at the median redshift of 0.43, with $M_{*,i}(z = 0.43) = -23.04$, this implies a bolometric luminosity $L_{\text{bol}} > 10^{38.5} \text{W}$. Assuming that the quasars are radiating at the Eddington rate [$L_{\text{Edd}} = 10^{39.1} (M_{\text{bh}}/10^8 M_{\odot}) \text{W}$], this implies black hole masses $M_{\text{bh}} > 3 \times 10^7 M_{\odot}$.

Table 1 summarizes the various subsamples we consider in this paper (discussed further in Section 3.2).

2.2 Luminous red galaxies

We cross-correlate the above quasars with a sample of LRGs selected from the SDSS imaging data. The sample selection, angular mask and redshift distributions have been described in detail in Padmanabhan et al. (2007), and we refer the reader to the details there. These galaxies have well-characterized photometric redshifts and errors ($\delta z \sim 0.03$), allowing us to deconvolve the photometric redshift distribution to obtain the underlying dN/dz (Padmanabhan et al. 2005). We consider LRGs with $0.25 < z_{\text{photo}} < 0.55$, trimmed to an angular mask that covers 3528.04deg^2 in the northern Galactic hemisphere; this results in a sample of 454 882 LRGs. We then divide the sample into six redshift ranges, summarized in Table 2, of photometric redshift width $\Delta z = 0.05$, where the redshift boundaries are chosen to select approximately homogeneous samples as the 4000\AA break shifts from the g to r band. We found that the LRG properties varied significantly over the redshift range making fine z_{photo} bins essential for proper modelling, the choice of $\Delta z = 0.05$ being determined by the photometric redshift errors. The LRG samples are summarized in Table 2, while the deconvolved redshift distributions are in plotted in Fig. 1.

Table 2. Properties of the LRG samples, showing the number, photo- z range, mean and modal redshift, width, growth factor (normalized to unity today) at the modal redshift, number density (in $10^{-4} h^3 \text{ Mpc}^{-3}$) and large-scale bias. We estimate the large-scale bias by fitting to $\omega(\theta_s)$ assuming scale-independent bias or fitting to a halo model (see the text). The quoted errors are purely statistical. The biases estimated from the different methods have systematic errors at the 5 per cent level. We adopt b_{halo} as our fiducial value.

Sample	n_{LRG}	$z_{\text{photo-range}}$	$\langle z \rangle$	z_{mode}	δz	D	\bar{n}	b_{constant}	b_{halo}
LRG1	29,660	$0.25 < z < 0.30$	0.276	0.287	0.029	0.87	4.7	1.75 ± 0.05	1.71 ± 0.05
LRG2	32,527	$0.30 < z < 0.35$	0.326	0.312	0.033	0.86	4.1	1.77 ± 0.06	1.77 ± 0.05
LRG3	41,051	$0.35 < z < 0.40$	0.376	0.375	0.049	0.84	3.4	2.36 ± 0.05	2.15 ± 0.07
LRG4	60,294	$0.40 < z < 0.45$	0.445	0.452	0.058	0.81	3.7	2.28 ± 0.05	2.09 ± 0.05
LRG5	104,131	$0.45 < z < 0.50$	0.506	0.488	0.048	0.79	4.7	2.02 ± 0.04	1.90 ± 0.04
LRG6	95,605	$0.50 < z < 0.55$	0.552	0.541	0.051	0.78	4.2	1.90 ± 0.05	1.76 ± 0.05

3 CLUSTERING

3.1 LRG clustering

3.1.1 Methods

We measure the clustering of the LRG sample in each of the six photometric redshift slices using the angular clustering estimator described in Padmanabhan, White & Eisenstein (2007). We define

$$\omega(\theta_s) \equiv 2\pi \int_0^{\theta_s} \theta d\theta G(\theta, \theta_s) w(\theta), \quad (4)$$

where

$$\theta_s^3 G(\theta, \theta_s) = (x^2)^2 (1 - x^2)^2 \left(\frac{1}{2} - x^2 \right) \quad x < 1, \quad (5)$$

$$= 0 \quad x \geq 1,$$

with $x = \theta / \theta_s$. As was shown in Padmanabhan et al. (2007), this estimator partially deprojects the angular correlation function, yielding a robust estimate of the 3D real-space correlation function on scales of $\sim \frac{1}{2} \bar{\chi} \theta_s$, where $\bar{\chi}$ is the mean comoving distance to the redshift slice under consideration.

We implement the above estimator using $DD/RR - 1$ as our estimate of the angular correlation function. Although the Landy & Szalay (1993) estimate is a more traditional choice, the contiguous wide-area coverage of the SDSS imaging makes it unnecessary in our case, and we choose the simpler estimator. Substituting this into equation (4), we obtain

$$\omega(\theta_s) = 2\pi \int \theta d\theta G(\theta, \theta_s) \frac{DD}{RR}, \quad (6)$$

where we use the fact that the area-weighted integral of $G(x)$ vanishes by construction. In order to proceed, we note that the RR term is a purely a geometric term determined by the survey mask. Although this is traditionally estimated by measuring random-random pairs in the same binning as the DD pairs, Padmanabhan et al. (2007) point out that on scales much smaller than the size of the survey, RR is described by

$$RR \propto 2\pi\theta \Delta\theta \Phi(\theta), \quad (7)$$

where $\Phi(\theta)$ is a smooth function; we obtain a good fit to Φ using a fifth-order polynomial. Having fit Φ , we can make our θ bins arbitrarily small without incurring any Poisson noise penalty. This allows us to rewrite equation (6) as a weighted sum over pairs:

$$\omega(\theta_s) = \sum_{i \in DD} \frac{G(\theta_i, \theta_s)}{\Phi(\theta_i)} \Theta(\theta_s - \theta_i), \quad (8)$$

where Θ is the Heaviside step function.

We estimate the covariance matrix of our measurements by bootstrap resampling (e.g. Efron & Gong 1983). An important advantage of $\omega(\theta_s)$ is its insensitivity to clustering on scales $\gtrsim 2\theta_s$. This allows us to subdivide the survey into 41 approximately filled spherical rectangles, 7:5 in the RA direction and 0.15 in the $\sin(\delta)$ direction. Computing $\omega(\theta_s)$ for each of these subsamples yields 41 independent, identically distributed realizations of $\omega(\theta_s)$. The independence of the subsamples is a direct consequence of the estimator; this is not true for the more traditional $w(\theta)$. We then estimate both the average and covariance matrix by bootstrap resampling these 41 realizations. In order to improve the numerical stability of this procedure, we scale ω by θ_s^2 , thereby removing the artificially large condition number of the covariance matrix that arises due to the large dynamic range of ω . The resulting covariance matrix is very well behaved, with no anomalously small modes that need to be removed. Note that this is not the case for $w(\theta)$ which is sensitive to large-scale fluctuations, which, in turn, lead to unphysical modes in the covariance matrix that must be further conditioned. The insensitivity of $\omega(\theta_s)$ to long wavelengths is an important advantage when attempting to estimate the covariance matrix from the data itself.

3.1.2 Results

The angular clustering of the LRGs in the six redshift slices is shown in Fig. 4, using the estimator described above; also plotted is the approximate physical scale probed by ω at a given θ_s . Note that the errors between different points are correlated, and we use the full covariance matrix in all fits.

Given the observed angular clustering, one can infer the underlying 3D clustering of the sample; we do this using two methods. The first assumes that the LRG clustering traces the dark matter with a scale-independent bias on large scales. We compute $\omega(\theta_s)$ assuming the Smith et al. (2003) prescription for the shape of the non-linear dark matter power spectrum, and estimate the large-scale bias by fitting the data on scales larger than 0.2, corresponding to physical scales $\gtrsim 2 h^{-1} \text{ Mpc}$. The best-fitting models are plotted in Fig. 4, with the corresponding bias values in Table 2. The Smith et al. (2003) prescriptions deviate from the observed clustering on small scales; as one might expect: LRGs do not trace the dark matter on these scales.

The second method attempts to model the observed clustering by fitting a halo occupation distribution (HOD), i.e. the average number of LRGs per halo as a function of halo mass; we refer the reader to Appendix A for details. The best-fitting ω are in Fig. 4, and the predicted large-scale bias values are in Table 2. Taking into account the likelihood of scale-dependent bias and the 5 per cent systematic

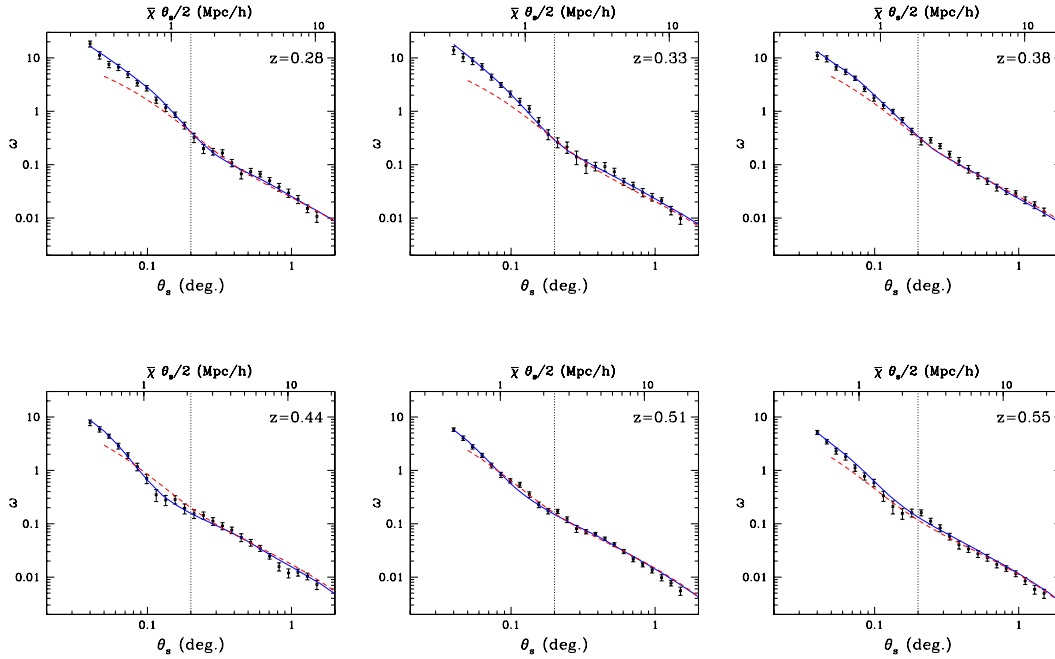


Figure 4. The observed ω for the six LRG redshift slices, as a function of the filter scale θ_s . Recall that ω probes the angular correlation function on scales $\sim \theta_s/2$; the corresponding physical scales are also shown. We also plot the best-fitting models, both from the Smith et al. (2003) fitting formula (dashed/red line) for the non-linear dark matter clustering, as well as from our halo model fits (solid/blue line). The dotted vertical line marks the angular scale beyond which we fit the HaloFit models. These fits deviate from the observed clustering on small scales; LRGs are not distributed like the dark matter on these scales. The halo model correlation functions are estimated from the same realizations in the $500 h^{-1}$ Mpc simulation that we use to interpret the quasar-LRG cross-correlations. Note that the data are well fit by the halo model on both small and large scales.

uncertainty in the halo modelling (see Appendix A), these are in reasonable agreement with the simple fits described above. The halo models (Fig. 5) reproduce the observed correlations well, including the prominent break in the correlation function (the best-fitting χ^2 values are in Table A1). Our LRG samples populate a broad range of halo masses, with an approximate power-law dependence of the mean number of LRGs per halo with the halo mass. Furthermore, we find that the haloes with masses $\sim 10^{13} M_\odot$ have one LRG in them. An important byproduct of this process is that we obtain mock realizations of the LRG sample; we use these below to interpret the clustering measurements of the quasars.

The LRG clustering amplitude is consistent with being non-evolving with redshift, implying a bias that evolves as $b(z) \sim 1/D(z)$. An exception is LRG3 and LRG4, which have a significantly higher bias. These slices straddle the transition between two different selection criteria, and the LRGs selected here have a higher luminosity than average, explaining the higher bias; this was discussed in detail by Padmanabhan et al. (2007). Comparing the bias values and HOD fits, we see that the LRGs can be conveniently grouped into three slices of width $\Delta z_{\text{photo}} = 0.1$, each of which samples a homogeneous population of galaxies.

Finally, we note our results are consistent with those of Padmanabhan et al. (2007) correcting for differences in the fiducial cosmologies. That paper also performed a number of systematic tests on the LRG sample, and we simply refer the reader to that work instead of repeating them here.

3.2 QSO clustering

3.2.1 Methods

The quasars in our sample have spectroscopic redshifts and thus we know (up to small uncertainties due to peculiar velocities) a

physical distance to each object. This allows us to work in terms of transverse separation rather than angular separation, i.e. to measure

$$w_p(R) \equiv \int d\Delta \chi \xi(\sqrt{R^2 + \Delta \chi^2}) \quad (9)$$

rather than $w(\theta)$ or its generalizations. As with the LRGs, this is a real-space measurement, avoiding the need to model redshift space distortions.

We start by considering quasars in a narrow redshift range (a comoving distance χ_0 away), and correlate them with LRGs with a normalized radial distribution, $f(\chi)$. In the flat sky approximation, the angular correlation function is given by

$$w(\theta) = \int d\chi f(\chi) \xi \left[\sqrt{\chi_0^2 \theta^2 + (\chi - \chi_0)^2} \right], \quad (10)$$

where the usual second integral over the quasar redshift distribution has been eliminated because the quasars have spectroscopic redshifts. We can now make the usual Limber (1953) approximation for $\chi_0 \theta$ much smaller than the scales over which $f(\chi)$ varies. This allows us to hold $f(\chi)$ fixed at $f(\chi_0)$ in the integral, yielding

$$\begin{aligned} w(\theta) &\simeq f(\chi_0) \int d\chi \xi \left[\sqrt{\chi_0^2 \theta^2 + (\chi - \chi_0)^2} \right] \\ &= f(\chi_0) w_p(R). \end{aligned} \quad (11)$$

Note the second use of the assumption of a peaked integral to re-extend the limits of the integral to $\pm\infty$. The second equality just recognizes the integral as the projected correlation function w_p at transverse separation $R = \chi_0 \theta$.

To generalize to a broad redshift slice, we start with the standard assumption that $w_p(R)$ does not evolve over the slice. One then has two choices – the first is to estimate $w(\theta)$ over narrow

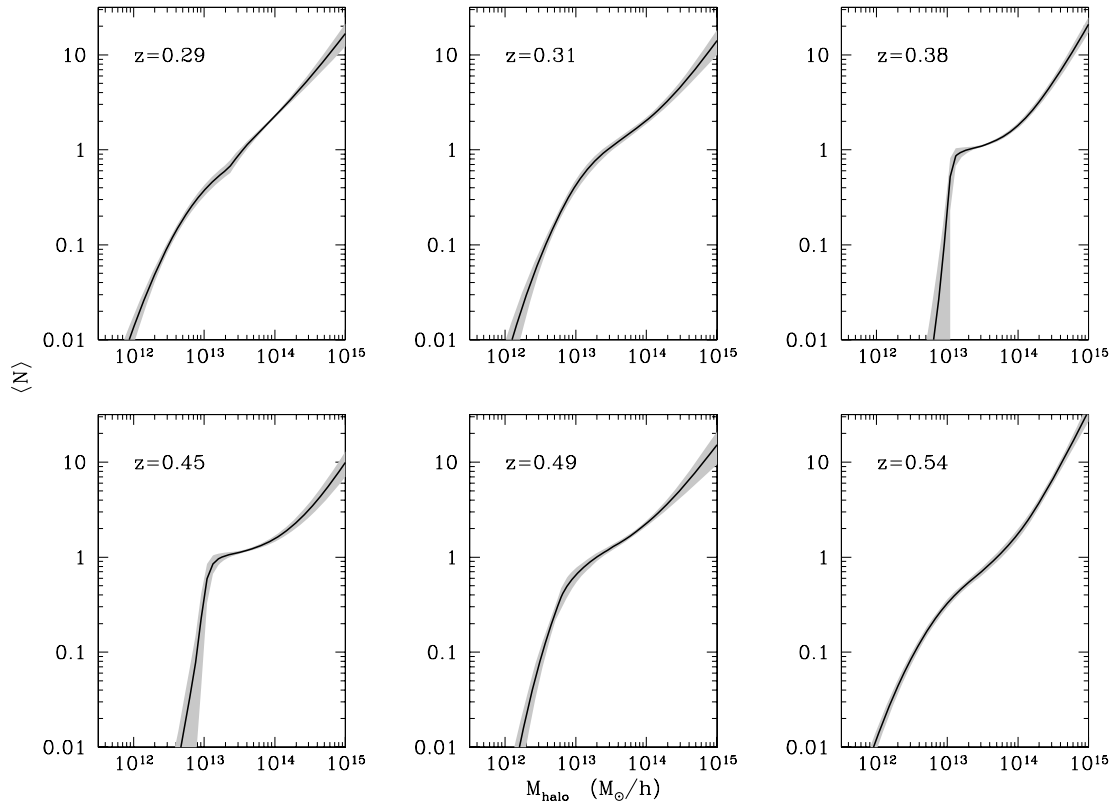


Figure 5. Best-fitting HODs for the six LRG slices we consider in this paper. The shaded region denotes the errors, as estimated by Monte Carlo.

redshift slices, estimate $w_p(R)$ for each of these slices using equation (12) and then average. This has the disadvantage that each individual $w_p(R)$ measurement is extremely noisy, and potentially sensitive to noise in $f(\chi)$. The other approach (which we adopt) makes use of the fact that θ in equation (12) is simply a label, and can just as easily be replaced by R . This has a simple interpretation – one computes the angular correlation function over the broad redshift range but replaces the angular separation by the transverse separation R computed assuming that the LRGs are the same redshift as the quasar being correlated with. We use the estimator:

$$w_\theta(R) = \frac{QG(R)}{QR(R)} - 1, \quad (13)$$

where QG and QR are the quasar–galaxy and quasar–random pairs, and our notation makes explicit that we are binning in physical transverse separation. Since we assume that $w_p(R)$ is constant over the redshift range, equation (12) yields

$$w_\theta(R) = \langle f(\chi) \rangle w_p(R), \quad (14)$$

where the average is done over the quasar redshift distribution. Note that this formulation both avoids the intermediate step of computing noisy estimates of $w(\theta)$ in narrow redshift slices and is less sensitive to noise in $f(\chi)$. Finally, we point out that, in equation (13), one only requires the angular selection function of the LRGs to estimate QR .

Note that one could use the estimator described by equation (4) to measure the cross-correlations. However, the lower signal-to-noise ratio of the quasar-LRG cross-correlations eliminates the advantages of the estimator, and therefore, we choose the simpler estimator.

Estimating the covariance matrix for our sample is simplified by the low number density of the quasars, making them effectively independent for the scales of interest. We therefore estimate the covariance matrix by simply bootstrapping the individual quasars. As with the LRGs, we remove the artificially large condition number by scaling $w_p(R)$ by R before estimating the covariance matrix. Finally, as a check, we note that we obtain consistent results if we replace the bootstrap covariance matrix with a jackknife estimate.

3.2.2 Results

In order to determine what subsamples to cross-correlate with, we start with the observation (see Section 3.1) that the LRGs can be grouped into three homogeneous slices of width 0.1 in photometric redshift, i.e. grouping slices (1, 2), (3, 4) and (5, 6) of Table 2 together. We use the mean redshift of each LRG redshift slice and its width to determine the redshift range of the quasars to cross-correlate with; this defines the redshift ranges of the quasar subsamples in Table 1. Note that since we use the true redshift distribution of the LRGs (as opposed to the photometric redshift distribution) to determine the mean and width of the slices, we automatically correct for any biases and asymmetries in the photometric redshift errors. For each of these three quasar redshift slices (denoted as ALL below), we further consider the following subsamples – the LSTAR sample defined in Section 2, restricting to quasars targeted with the latest version of the SDSS target selection algorithm, and a bright and faint subsample split at the median luminosity for each redshift slice.

As anticipated earlier, we find that restricting to the latest version of the SDSS target selection algorithm gives the same cross-clustering power against the LRGs as the ALL sample; we therefore

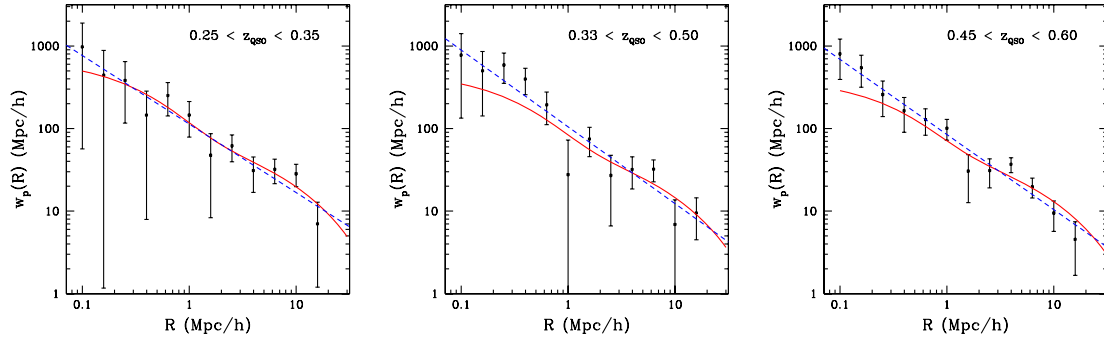


Figure 6. The observed $w_p(R)$ measuring the cross-correlation between quasars and the LRG samples. The solid (red) line shows the HaloFit prescription for the non-linear dark matter correlation function, normalized by a scale-independent bias to best fit the observed correlations. The dashed (blue) line shows the best-fitting power-law model.

Table 3. The large-scale quasar bias and power-law fits for the ALL and LSTAR samples. We fit scales $R > 2 h^{-1}$ Mpc (5 points) for the bias and all scales (12 points) for the power-law model. The second column lists the LRG slice assumed for the bias (see the text and Table 2 for details), while the third and fourth columns list the amplitude of the quasar-LRG cross-correlation and the implied (scale-independent) bias, assuming a dark matter $\xi(r)$ given by the Smith et al. (2003) model. Note that we ignore the contribution of the error in the LRG bias in the derived QSO bias. The best-fitting r_0 and γ values are listed under r_0 and γ , while likelihood-averaged values are under $\langle r_0 \rangle$ and $\langle \gamma \rangle$. Note that the errors in r_0 and γ are correlated; the cross-correlation coefficient is under r .

Sample	LRG Sample	$b_{\text{QSO}} b_{\text{LRG}}$	b_{QSO}	χ^2	r_0 (Mpc/h)	γ	$\langle r_0 \rangle$ (Mpc/h)	$\langle \gamma \rangle$	r	χ^2
ALL0	1	2.73 ± 0.45	1.60 ± 0.26	1.78	6.70	1.71	6.48 ± 0.63	1.70 ± 0.10	0.18	8.01
ALL1	3	2.56 ± 0.47	1.17 ± 0.22	4.03	6.44	1.82	6.29 ± 0.54	1.81 ± 0.09	-0.30	6.70
ALL2	5	2.30 ± 0.38	1.20 ± 0.19	2.86	5.56	1.82	5.46 ± 0.42	1.82 ± 0.08	-0.28	5.94
LSTAR0	1	2.50 ± 0.62	1.46 ± 0.37	3.88	6.60	1.83	6.23 ± 0.90	1.82 ± 0.15	-0.13	7.42
LSTAR1	3	2.12 ± 0.64	0.96 ± 0.29	4.54	6.00	1.93	5.75 ± 0.79	1.92 ± 0.14	-0.49	10.22
LSTAR2	5	2.08 ± 0.41	1.08 ± 0.20	5.15	5.42	1.91	5.29 ± 0.48	1.91 ± 0.09	-0.44	8.68

do not trim the sample based on the version of the target selection algorithm. Furthermore, as is evident from Fig. 3, the luminosity baseline is rather small, and no clear trend with luminosity emerges, given our errors; this prevents us from subdividing into subsamples based on luminosity. The higher redshift slices do not extend significantly below L_* , so to simplify the interpretation we use the LSTAR sample as our fiducial sample. Fig. 6 plots the cross-correlations for the LSTAR sample.

We present both power-law and large-scale bias fits to both these subsamples. In order to estimate the mean and error for any parameter p (possibly a vector), we use

$$\langle p \rangle = \frac{\int d\mathbf{p} \mathcal{L}(\mathbf{p}) \mathbf{p}}{\int d\mathbf{p} \mathcal{L}(\mathbf{p})} \quad (15)$$

and

$$\sigma_{p_i}^2 = \langle p_i^2 \rangle - \langle p_i \rangle^2, \quad (16)$$

where the likelihood is defined by $\mathcal{L} \equiv \exp(-\chi^2/2)$, with χ^2 computed using the full covariance matrix. For the power-law fits, we adopt a two parameter model:

$$\frac{w_p(R)}{R} = \frac{\sqrt{\pi} \Gamma[(\gamma - 1)/2]}{\Gamma(\gamma/2)} \left(\frac{r_0}{R} \right)^\gamma, \quad (17)$$

which corresponds to a 3D cross-correlation of the form $\xi(r) = (r/r_0)^{-\gamma}$. We fit this model to the measured correlations on all scales. In order to determine the large-scale bias, we compute $w_p(R)$ for the dark matter at $z = 0.3, 0.42$ and 0.53 using the prescription in Smith et al. (2003). This is then scaled by an R -independent multiplier to obtain the best fit to the data in the range $R > 2 h^{-1}$ Mpc. In the limit of scale independent, deterministic bias the multiplier is $b_Q b_{\text{LRG}}$ (see Table 3 for the values). We transform these into b_Q by using b_{LRG} for slices 1, 3 and 5, scaled to the corresponding redshift by the growth

factor. Note that the LRG clustering amplitude is close to constant with redshift, so we would obtain consistent numbers if we had used the other slices. The lower limit in the fit, $2 h^{-1}$ Mpc, was determined by the scale at which $w_p(R)$ from QSO-LRG cross-correlations in our mock catalogues (see Section 4.2) showed significant scale-dependent bias.

The results for the large-scale bias and power-law fits are in Table 3, while Fig. 7 plots the evolution of the clustering amplitude of the LSTAR sample as a function of redshift. Our results are consistent with a constant clustering amplitude from $z = 0.25$ to 0.6 , corresponding to a bias of 1.09 ± 0.15 at $z = 0.43$.

Table 4 summarizes our results compared with previously published work.¹ Our results strongly favour the general consensus that the bias of low-redshift quasars is ~ 1 ; this is also consistent with the models of Hopkins et al. (2007) as well as the previous extrapolations by Croom et al. (2005). There are two significant exceptions – Myers et al. (2007a) find 1.93 ± 0.14 based on a photometrically selected sample of quasars. It is possible that contamination by a high-redshift population could boost the measured bias values. The more intriguing discrepancy is with Mountrichas et al. (2009) who analyse a similar sample to ours, also in cross-correlation with LRGs, and find biases between 1.90 ± 0.16 and 1.45 ± 0.11 depending on the particular LRG and quasar sample they cross-correlate against. These results are also discrepant with da Angela et al. (2008) – with whom we are consistent – who analyse the same sample in autocorrelations. Furthermore, the scatter in the different subsamples analysed by Mountrichas et al. (2009)

¹ We do caution the reader that the errors for a number of these measurements are simply Poisson errors, and ignore correlations between different scales and are therefore likely underestimated.

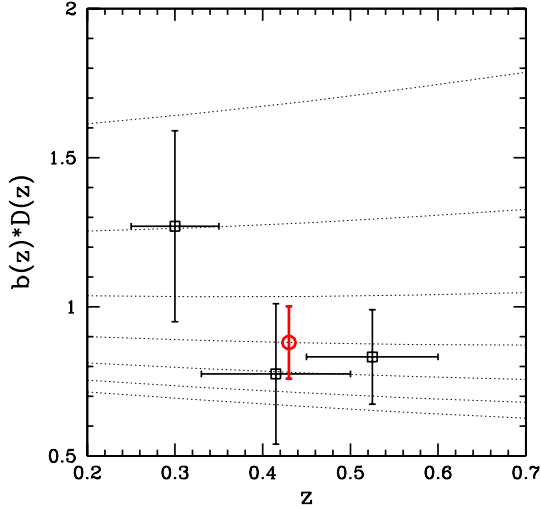


Figure 7. The bias of the three LSTAR quasar subsamples (squares) as a function of redshift, as well as the mean bias (circle). We consider the bias scaled by the growth factor to focus on the evolution of the clustering amplitude. Also plotted (dashed lines) is the bias of haloes with masses (from bottom to top panel) ranging from $\log_{10}(M/M_{\odot})$ of 10.5 to 13.5 in steps of $d \log_{10}(M/M_{\odot}) = 0.5$. Note that the mean large-scale bias of 1.09 ± 0.15 at $z = 0.43$ suggests that quasars live in haloes of mass $\sim 10^{12} h^{-1} M_{\odot}$.

Table 4. A summary of previous low-redshift quasar clustering results, compared with results in this work, scaled to the cosmology assumed here. (1) This work, (2) Croom et al. (2005), (3) Myers et al. (2007a), (4) Coil et al. (2007), (5) da Angela et al. (2008), (6 and 7) Mountrichas et al. (2009) and (8) Croom et al. (2004). For the results from Coil et al. (2007), we scale the relative bias presented there by the large-scale bias $b = 1.22$ of all DEEP2 galaxies (Zheng, Coil & Zehavi 2007).

z	L_{\min}	b_{QSO}	References
$0.25 < z < 0.6$	L_{*}	1.09 ± 0.15	(1)
$0.3 < z < 0.68$	$0.4L_{*}$	1.27 ± 0.20	(2)
$0.4 < z < 1.0$	$0.1L_{*}$	1.93 ± 0.14	(3)
$0.7 < z < 1.4$	$0.1L_{*}$	1.09 ± 0.29	(4)
$z \sim 0.6$	$0.4L_{*}$	1.10 ± 0.20	(5)
$z \sim 0.6$	$0.4L_{*}$	1.90 ± 0.16	(6)
$z \sim 0.6$	$2.5L_{*}$	1.45 ± 0.11	(7)
$z < 0.3$	$0.4L_{*}$	0.97 ± 0.05	(8)

significantly exceeds their quoted errors, suggesting either a systematic in their analysis or an underestimate of their errors. Using the observed scatter between the different subsamples as an estimate of the error yields a value consistent with our measurement. Finally, two results not presented in Table 4 are Serber et al. (2006) and Strand et al. (2008). There are a number of subtleties while interpreting these results (resulting in misunderstandings in the literature); we therefore defer a detailed discussion of these results to Appendix B.

4 INTERPRETATIONS

4.1 The large-scale bias

The large-scale bias of any population of objects provides information on the mean dark matter haloes mass hosting that population. Specifically, if $N(M_h)$ is the mean number of possible QSO hosting galaxies (i.e. galaxies with black holes massive enough to fuel

QSOs) hosted by a halo of mass M_h then

$$\bar{n} = \int dM_h \frac{dn_h}{dM_h} N(M_h), \quad (18)$$

$$\langle b \rangle = \bar{n}^{-1} \int dM_h \frac{dn_h}{dM_h} b_h(M_h) N(M_h), \quad (19)$$

where dn_h/dM_h is the (comoving) number density of haloes per mass interval (e.g. Sheth & Tormen 1999) and $b_h(M_h)$ is the bias associated with haloes of that mass (e.g. Cole & Kaiser 1989; Sheth & Tormen 1999; Sheth, Mo & Tormen 2001). Note that $\langle b \rangle$ is independent of the normalization of $N(M_h)$. Also, since observable quasar activity is a transient property, the observed quasar number density \bar{n}_{QSO} depends upon the average duty cycle, f_{on} ,

$$\bar{n}_{\text{QSO}} = f_{\text{on}} \bar{n}. \quad (20)$$

To set the scale, Fig. 7 compares the observed large-scale bias with that of haloes of fixed mass in our assumed cosmology. Our data are consistent with host haloes having a mass $10^{11.5} - 10^{12.5} h^{-1} M_{\odot}$, in agreement with earlier work (Porciani et al. 2004; Croom et al. 2005; Lidz et al. 2006; Porciani & Norberg 2006).² Note that our constraints are significantly stronger for higher as opposed to lower halo masses, since $b_h(M)$ is a rapidly rising function above $\sim 10^{13} h^{-1} M_{\odot}$ but slowly asymptotes to a constant ($b \sim 0.5$) for lower masses. As we see no evidence for evolution in the QSO bias, we use the mean value from all three slices below.

However, we do not expect QSOs to inhabit haloes of a single mass. To place constraints on the range of haloes in which quasars may be active, we consider two illustrative models. First, we imagine that QSOs brighter than L_{*} live in haloes more massive than M_{\min} , with each halo above M_{\min} hosting exactly one QSO with probability f_{on} . This gives $N(M_h) = \Theta(M_h - M_{\min})$, where the Heaviside Θ function is unity for positive arguments and zero otherwise. Fig. 8 and Table 5 summarize the constraints on this model. As anticipated by our simple scaling argument above, our measurements suggest $M_{\min} \sim 10^{11} h^{-1} M_{\odot}$ corresponding to an average halo mass $\langle M \rangle \sim 10^{12} h^{-1} M_{\odot}$. We further strongly disfavour models with $M_{\min} \gg 10^{12} h^{-1} M_{\odot}$. Our lower mass limits are significantly weaker for the reasons discussed above, requiring $M_{\min} > 10^{9.5} h^{-1} M_{\odot}$, with even lower masses still providing marginally acceptable fits. However, such masses are disfavoured by the locally observed $M_{\text{bh}} - \sigma$ relation (Ferrarese & Merritt 2000; Tremaine et al. 2002). Assuming an Eddington-limited accretion rate, the LSTAR sample should be powered by the black holes with masses $M_{\text{bh}} > 10^7 h^{-1} M_{\odot}$, which live in bulges with $\sigma \sim 100 \text{ km s}^{-1}$ or M_{bulge} a few times $10^9 h^{-1} M_{\odot}$. Given mass-to-light ratios of a few, this disfavours $M_{\min} < 10^{10} h^{-1} M_{\odot}$.

The second model we consider starts from the assumption that QSOs cluster like a random sampling of a luminosity or colour subsample of galaxies. This motivates a form,

$$N(M_h) = \Theta(M - M_{\min}) \left[1 + \left(\frac{M}{20M_{\min}} \right)^{\alpha} \right], \quad (21)$$

found to be a good description of galaxies at both low and high redshifts (e.g. Zehavi et al. 2005; Conroy, Wechsler & Kravtsov 2006; White et al. 2007). This has a central galaxy in all haloes above M_{\min} and on average $(M/20M_{\min})^{\alpha}$ satellites in each halo,

² A little appreciated uncertainty in this conversion comes from differences in fitting functions to $b_h(M)$ resulting in an additional error of 50 per cent (0.2 dex) in mass.

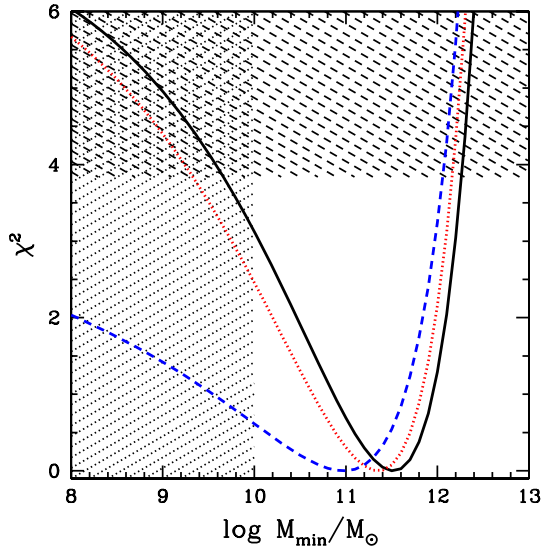


Figure 8. M_{\min} for the threshold (solid, black line) and galaxy-like $\alpha = 0.5$ (dotted, red line) and $\alpha = 0.9$ (dashed, blue line) HODs, as constrained by the average large-scale bias of the LSTAR sample. The dotted hatched region marks the region disfavoured by quasar lifetimes and the $M_{\text{bh}}-\sigma$ relation. The dashed hatched region is excluded at 95 per cent confidence. See the text for more details.

Table 5. Halo masses derived from the average large-scale bias of our QSO sample. The masses are quoted in units of $10^{12} h^{-1} M_{\odot}$. The different HOD models are described in detail in the text. The superscript 95 refers to the 95 per cent cl upper limits.

HOD	M_{\min}	$\langle M \rangle$	M_{\min}^{95}
Threshold	0.3	1.9	2.0
$\alpha = 0.5$	0.3	3.1	1.6
$\alpha = 0.9$	0.1	6.1	1.3

where the factor of 20 is inspired by fits to SDSS galaxies and N -body simulations. We consider cases with $\alpha = 0.5$ and 0.9 ; the former to model blue galaxies (which are under-represented in high-mass haloes) and the latter to describe a luminosity selected sample. (The models are supposed to be illustrative.) As before, a fraction f_{on} of the QSOs are ‘on’ at the time of the observation. Fig. 8 and Table 5 again summarize the constraints from the large-scale bias, which are very similar to those obtained for the threshold models. Within the context of this model, we can translate this into a constraint on the space density of quasar hosts and hence on their luminosity. The preferred value of M_{\min} suggests $\bar{n} \simeq 5 \times 10^{-2} h^3 \text{Mpc}^{-3}$ or a luminosity $L < 0.1 L_*$ using the blue-galaxy LF of Faber et al. (2007). The 95 per cent confidence level upper limit on b gives $\bar{n} \simeq 4 \times 10^{-3} h^3 \text{Mpc}^{-3}$ or a luminosity $L \sim L_*$. The number density at fixed bias is lowered if we allow scatter in the L – M relation (i.e. a smooth turn on in equation 21), as is likely. With lognormal scatter in M at fixed L of $\sigma_{\ln M} = 1$, the space density is reduced by a factor of ~ 4 at fixed bias and the upper limit on the threshold luminosity becomes $1.1 L_*$ (cf. White, Martini & Cohn 2008). Using the stellar mass functions in Bundy et al. (2007), we find that these number densities correspond to stellar masses $M_{\star} < 2 \times 10^{11} h^{-1} M_{\odot}$. Of course, QSO hosts may not inhabit haloes in the manner assumed by equation (21). If QSO hosts are

under-represented in intermediate-mass haloes then it is possible to have a lower number density and $b \simeq 1$. This is what is seen in, for example, a sample of galaxies with $M_B < -21$ and a star formation rate $> 1 M_{\odot} \text{yr}^{-1}$ in the Millennium simulation (Springel et al. 2005; Croton et al. 2006; De Lucia & Blaizot 2007). The HOD of these galaxies is approximately described by a lognormal distribution peaking at $M \sim 10^{12} h^{-1} M_{\odot}$, with a power-law distribution at high masses. There is, however, a deficit of galaxies at $\sim 10^{13} h^{-1} M_{\odot}$; this allows one to have a low number density, without a high bias. Note that while our data are unable to constrain such flexible models, a large fraction of this uncertainty derives from the fact that the QSO number density does not add any constraints to the HOD.

Given the above models and caveats, and the observed space density of quasars, we constrain the duty cycle (equation 20) to be $< \mathcal{O}(10^{-3})$, consistent with the estimates by Dunlop et al. (2003) from the luminosity function. Converting the duty cycle, f_{on} , into a lifetime is somewhat ill defined. If we assume $t_Q = f_{\text{on}} t_h$, with t_h the Hubble time, we find $t_Q < 10^7 \text{yr}$. These lifetimes are broadly consistent with those derived at $z \sim 2$. On the other hand, the Hubble time is significantly longer and the duty cycles are significantly lower.

The exact time-scale to use in the above conversion is not well defined; our choice of the Hubble time for the halo lifetime is an approximation (see e.g. Martini & Weinberg 2001, for a different approximation). The differences between the various choices are of the same order of magnitude as the systematics in modelling the quasar host number density, and we therefore opt for simplicity. We, however, caution the reader that these numbers should only be treated as order-of-magnitude estimates.

If QSOs are radiating at the Eddington limit L_{edd} , then the minimum M_{bh} in our LSTAR sample is $3 \times 10^7 M_{\odot}$. This value is consistent with the estimates from the $M_{\text{bh}}-M_{\text{halo}}$ relation (Ferrarese 2002), $M_{\text{bh}} \sim 2 \times 10^7 - 3 \times 10^9 M_{\odot}$, with the differences coming from different assumptions about the halo profiles. This suggests $L/L_{\text{edd}} \sim 0.01 - 1$, consistent with the results of Croom et al. (2005) and da Angela et al. (2008), although we find no evidence of super-Eddington accretion.

4.2 Small-scale clustering

Due to the larger number density of LRGs with which we have cross-correlated our QSOs, we are able to measure the clustering down to smaller scales than would otherwise have been possible. Interpreting the small-scale clustering is, however, complicated by the uncertain relation between the galaxies which host active QSOs, the galaxies which are selected as LRGs and their parent host haloes. A full interpretation would require knowledge of the joint distribution $P(N_{\text{QSO}}, N_{\text{LRG}} | M_h)$, which cannot be meaningfully constrained with the limited data we have available. It is, however, straightforward, with the aid of the mock catalogues described previously, to predict the cross-clustering for any well-specified QSO scenario. In this section, we examine the illustrative models introduced in the last section, focussing on the $z \simeq 0.5$ data for definiteness.

We begin with the model in which QSOs are hosted exclusively by the central galaxies of haloes above some threshold M_{\min} . As with all of the models, we will ignore the number density constraint by postulating that a random fraction, f_{on} , of the possible hosts are seen as QSOs at any given time. If the probability of a host being on is independent of the host properties, the clustering is unchanged and we can use the host population – with its better statistics – to compute w_p . We find that this model cannot simultaneously account for the measured large-scale bias and the large amplitude

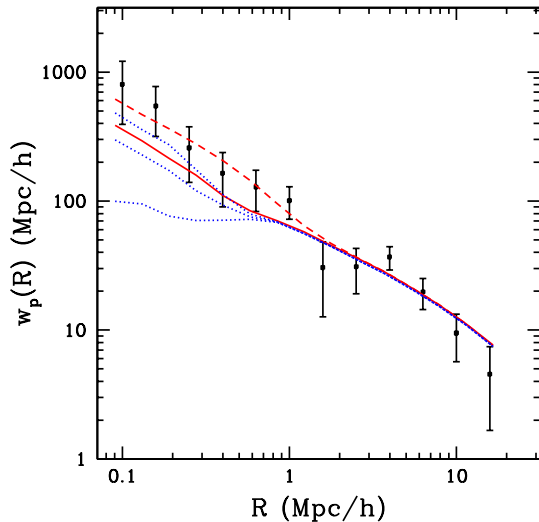


Figure 9. Comparison of the cross-correlation of simulated LSTAR2 and LRG5 samples with the observations. The solid ($\chi^2 = 12.7$) and dashed ($\chi^2 = 8.1$) lines assume a galaxy type $N(M_h)$ with $\alpha = 0.3$ and 0.9 , respectively, while the dotted lines (bottom to top panel) assume a threshold $N(M_h)$ with a mass-independent satellite fraction of 0 , 0.5 and 1 ($\chi^2 = 19.8$, 15.0 and 11.7 , respectively). We fix M_{\min} to the best-fitting values in Table 5; note that the large-scale clustering for all the models are identical. The χ^2 values are computed using all 12 points and the full covariance matrix.

of the small-scale correlation function (see the lowest dotted line in Fig. 9). To fit the former, the mean QSO-weighted halo mass must be low, but such low-mass haloes contain only central LRGs, not satellites, so there are no QSO–LRG pairs with separations $\mathcal{O}(100 h^{-1} \text{ kpc})$. We can keep the halo occupancy the same but distribute the QSOs within the haloes as both centrals and satellites. We assume satellites follow an NFW profile (Navarro, Frenk & White 1996) with a concentration of 10 – the precise details do not matter for our purposes, other choices produce qualitatively similar results and trends. By making 50 per cent of the QSOs satellites, we boost the power on small scales (Fig. 9), as it is now possible to have QSO–LRG pairs in the smaller, lower mass haloes.

We can also take the form of equation (21), imagining that a random sample of galaxies will host QSOs at the time of observation. We place a central galaxy in all haloes above M_{\min} and place a Poisson number of satellites, with mean $(M/20M_{\min})^\alpha$, distributed like a $c = 10$ NFW profile. The large-scale bias is again set by the mean halo mass, which is larger for larger α at fixed M_{\min} . As α is increased, the spread in small-scale clustering amplitude with M_{\min} decreases, with models lying very close to the data. A model with $\alpha \simeq 0.9$ (solid line in Fig. 9) gives very good fits, with $\chi^2/\text{d.o.f.} < 1$, when $M_{\min} \sim 10^{11} h^{-1} M_\odot$ but lower values of α (dashed line in Fig. 9) are not excluded. Due to the strong covariance between the $w_p(R)$ points, the constraint on M_{\min} from the full model is not stronger than that from just the large-scale points.

5 CONCLUSIONS

We measure the small-scale clustering of a sample of $\sim 400\,000$ photometric LRGs and their clustering around a volume-limited sample of ~ 2000 $z < 0.6$ low-redshift QSOs. By using a new statistical estimator, we are able to obtain precise measurements of the LRG angular correlation function, which coupled with their precise

and well-characterized photometric redshifts, allowed us to constrain how LRGs populate dark matter haloes. We find that LRGs have a clustering amplitude that is consistent with not evolving with redshift, and corresponding to a large-scale bias $b \sim 2$ at $z = 0.5$. The best-fitting halo occupation models suggest that they occupy haloes $> 10^{12} h^{-1} M_\odot$, with approximately one LRG in every $10^{13} h^{-1} M_\odot$ halo. We use these HODs to construct mock catalogues of LRGs. Attempting to match the observed cross-correlation of LRGs with QSOs by populating these same mock catalogues with QSOs allowed us, for the first time, to start to probe how quasars inhabit dark matter haloes.

Correlations with LRGs. The cross-correlation of QSOs and LRGs is well described on all measured scales by a power law of slope $\sim 1.8 \pm 0.1$ and a scalelength of $\sim 6 \pm 0.5 h^{-1} \text{ Mpc}$, consistent with observed slopes and amplitudes for local galaxies. It is also well described by the non-linear matter correlation function, scaled by a constant bias, although there is some evidence for deviations from this form at the smallest scales. Such deviations from the matter correlation function are, however, not unexpected, and are seen for most galaxy samples, which are better described by power laws down to small scales. Since this is in apparent contradiction with the results of Serber et al. (2006) and Strand et al. (2008), we revisit their measurement within the framework of cross-correlations developed in this paper (Appendix B). We explicitly show that their data are fit by a power law of slope 1.9 , with no deviations on small scales, and that the claims of an excess come from subtleties in interpreting their measurements.

QSO bias. The large-scale bias $b = 1.09 \pm 0.15$ is consistent with most previous measurements and theoretical models, the exceptions being Myers et al. (2007a) and Mountrichas et al. (2009); possible reasons for this discrepancy are discussed in Section 3.2.2. We see no evidence for variations of the bias with redshift or luminosity. The observed large-scale bias constrains quasars to reside in haloes with a mean mass of $10^{12} h^{-1} M_\odot$, with uncertainties of a factor of a few from the details of how the haloes are actually populated. Our constraints on the halo mass are significantly stronger from above than below, since these haloes are below the non-linear mass scale and occupy the slowly varying region of the halo bias curve. This should be contrasted with measurements at higher redshifts; even though the characteristic halo mass is the same at these redshifts (da Angela et al. 2008), it is now higher than the non-linear mass and probes the steeply rising part of the halo bias curve. This problem is exacerbated when one considers realistic models of halo occupation.

Halo masses, lifetimes, Eddington ratios. The mean halo mass can, in turn, be used to constrain the lifetimes of these QSOs (Cole & Kaiser 1989; Haiman & Hui 2001; Martini & Weinberg 2001) to be $< 10^7$ yr. This is consistent with the measurements at high redshift; on the other hand, the Hubble time is significantly longer in the local Universe, and therefore the duty cycles are significantly shorter. We also discuss some of the theoretical uncertainties in estimating the number density of quasar hosts (and therefore the duty cycles and lifetimes), which arise from the difficulties in constraining how quasars populate dark matter haloes. We find the number densities of quasar hosts are only certain at the order of magnitude level, obviating any need for the detailed modelling (popular in the literature) of the conversion of number densities into quasar lifetimes.

Assuming local $M_{\text{bh}}\text{--}M_{\text{halo}}$ relations (Ferrarese 2002), we estimate Eddington ratios between 0.01 to 1 . We do not find any need for super-Eddington accretion, in contrast with da Angela et al. (2008) who require super-Eddington ratios under certain assumptions for the halo profile. However, the errors on both the

measurements are large, and are therefore consistent with each other. These Eddington ratios are also consistent with the measurements at $z \sim 2$, suggesting no evolution in the Eddington ratio with redshift.

Satellite Fractions. Given our detailed modelling of the LRG clustering and the associated mock catalogues, we attempt to use the small-scale cross-correlation to constrain how quasars must populate dark matter haloes. The size of our errors precludes being able to place interesting constraints on general quasar models. However, the forward modelling problem – taking a particular quasar model, and comparing it with our data – is straightforward. We find that our small-scale measurements are inconsistent with quasars being a random subsample of all halo centres above a certain mass threshold, but become consistent if we assume >25 per cent of the quasars are satellites. We also find that our data are extremely well fit, if we assume that quasars are a random subsampling of luminosity-threshold sample of galaxies, for luminosity thresholds between $0.1L_*$ and L_* . The above results suggest that the host galaxies have a number density $<10^{-3} h^3 \text{Mpc}^{-3}$, corresponding to stellar masses $M_* < 10^{11} h^{-1} M_\odot$; the exact values are, however, sensitive to the particular choice of model.

Implications for future modelling. A second purpose of this paper was to demonstrate the modelling of how quasars populate dark matter haloes. An interesting question therefore is how to optimize future measurements to gain the most leverage on this. Modelling QSO–galaxy cross-correlations differs from the traditional galaxy–galaxy autocorrelations in two important ways. The first is the lack of a constraint on the number density of the underlying population that quasars are assumed to sample, which usually puts a strong constraint on the minimum halo mass. For quasars, such a constraint must come from the bias and as discussed above this is only strongly constraining when one is on the steeply rising part of the halo bias curve. The second difference is that the one-halo term is only probed where the QSOs and galaxies occupy the same haloes. For the quasar and LRG sample presented here, the mean halo mass for the quasars probes only the tail of the LRG HOD, making the constraints weaker than one might naively expect. On the other hand, we emphasize that the accurate and well-characterized photometric redshifts of the LRGs were an essential prerequisite for doing the modelling in the first place – this could not have been done with the full SDSS photometric sample. This suggests that a better photometric sample to correlate with would be a fainter sample of red galaxies. These would retain the accurate photometric redshifts of our sample, but would probe the lower halo masses associated with quasars. Another possibility would be a sample of emission-line galaxies. These galaxies have the advantage of being likely physically associated with quasars, but the disadvantage that they would require a spectroscopic survey (since photometric redshifts would not be accurate enough), making it harder to survey large volumes. Furthermore, the modelling would be significantly easier at higher redshifts, where the quasar bias is higher. Various combinations of these will be available with the next generation of imaging surveys, making it possible to significantly improve on the constraints presented here.

ACKNOWLEDGMENTS

This paper benefited from discussions with Paul Martini and John Silverman. The authors acknowledge the Aspen Center for Physics for hosting a workshop on galaxy clustering in Summer 2007, where this work was conceived and begun. NP and MW thank the Center

for Cosmology and AstroParticle Physics at Ohio State University for their hospitality. NP is supported by a Hubble Fellowship HST-HF-01200.01 awarded by the Space Telescope Science Institute, which is operated by the Association of Universities for Research in Astronomy, Inc., for NASA, under contract NAS 5-26555. MW is supported by NASA and the DOE. PN is supported by a PPARC-STFC PDRA fellowship at the IfA. This work was supported by the Director, Office of Science, of the US Department of Energy under contract no. DE-AC02-05CH11231. The simulations used in this paper were performed on the supercomputers at the National Energy Research Scientific Computing center.

Funding for the SDSS and SDSS-II has been provided by the Alfred P. Sloan Foundation, the Participating Institutions, the National Science Foundation, the US Department of Energy, the National Aeronautics and Space Administration, the Japanese Monbukagakusho, the Max Planck Society and the Higher Education Funding Council for England. The SDSS Web Site is <http://www.sdss.org>.

The SDSS is managed by the Astrophysical Research Consortium for the Participating Institutions. The Participating Institutions are the American Museum of Natural History, Astrophysical Institute Potsdam, University of Basel, University of Cambridge, Case Western Reserve University, University of Chicago, Drexel University, Fermilab, the Institute for Advanced Study, the Japan Participation Group, Johns Hopkins University, the Joint Institute for Nuclear Astrophysics, the Kavli Institute for Particle Astrophysics and Cosmology, the Korean Scientist Group, the Chinese Academy of Sciences (LAMOST), Los Alamos National Laboratory, the Max-Planck-Institute for Astronomy (MPIA), the Max-Planck-Institute for Astrophysics (MPA), New Mexico State University, Ohio State University, University of Pittsburgh, University of Portsmouth, Princeton University, the United States Naval Observatory and the University of Washington.

REFERENCES

- Adelberger K. L., Steidel C. C., 2005a, *ApJ*, 627, L1
- Adelberger K. L., Steidel C. C., 2005b, *ApJ*, 630, 50
- Adelman-McCarthy J. et al., 2007, *ApJS*, in press
- Bahcall J. N., Kirhakos S., Saxe D. H., Schneider D. P., 1997, *ApJ*, 479, 642
- Boyle B. J., Shanks T., Croom S. M., Smith R. J., Miller L., Loaring N., Heymans C., 2000, *MNRAS*, 317, 1014
- Bundy K. et al., 2007, *ApJ*, 681, 931
- Coil A., Hennawi J. F., Newman J. A., Cooper M. C., Davis M., 2007, *ApJ*, 654, 115
- Cole S., Kaiser N., 1989, *MNRAS*, 237, 1127
- Conroy C., Wechsler R. H., Kravtsov A. V., 2006, *ApJ*, 647, 201
- Cooray A., Sheth R., 2002, *Phys. Rep.*, 372, 1
- Croom S. M. et al., 2004, in Richards G. T., Hall P. B., eds, *ASP Conf. Ser.* 311, *AGN Physics with the Sloan Digital Sky Survey*. Astron. Soc. Pac., San Francisco, p. 457
- Croom S. M. et al., 2005, *MNRAS*, 356, 415
- Croton D. J. et al., 2006, *MNRAS*, 365, 11
- da Angela J. et al., 2008, *MNRAS*, 383, 565
- Davis M., Efstathiou G., Frenk C. S., White S. D. M., 1985, *ApJ*, 292, 371
- De Lucia G., Blaizot J., 2007, *MNRAS*, 375, 2
- Dunlop J. S., McLure R. J., Kukula M. J., Baum S. A., O’Dea C. P., Hughes D. H., 2003, *MNRAS*, 340, 1095
- Efron B., Gong G., 1983, *Am. Stat.*, 37, 36
- Faber S. et al., 2007, *ApJ*, 665, 265
- Ferrarese L., 2002, *ApJ*, 578, 90
- Ferrarese L., Merritt D., 2000, *ApJ*, 539, L9
- Floyd D. J. E., Kukula M. J., Dunlop J. S., McLure R. J., Miller L., Percival W. J., Baum S. A., O’Dea C. P., 2004, *MNRAS*, 355, 196

Haiman Z., Hui L., 2001, *ApJ*, 547, 27
 Heitmann K. et al., 2008, *Comput. Sci. Discovery*, 1, 015003
 Hennawi J. F. et al., 2006, *AJ*, 131, 1
 Hopkins P. F., Lidz A., Hernquist L., Coil A. L., Myers A. D., Cox T. J., Spergal D. N., 2008, *ApJ*, 662, 110
 Kormendy J., Richstone D., 1995, *ARA&A*, 33, 581
 Landy S. D., Szalay A. S., 1993, *ApJ*, 412, 64
 Letawe G., Magain P., Courbin F., Jablonka P., Jahnke K., Meylan G., Wisotzki L., 2007, *MNRAS*, 378, 83
 Letawe Y., Magain P., Letawe G., Courbin F., Hutsemékers D., 2008, *ApJ*, 679, 967
 Lidz A., Hopkins P. F., Cox T. J., Hernquist L., Robertson B., 2006, *ApJ*, 641, 41
 Limber D. N., 1953, *ApJ*, 117, 134
 Lukic Z., Heitmann K., Habib S., Bashinsky S., Ricker P. M., 2007, *ApJ*, 671, 1160
 Lynden-Bell D., 1969, *Nat*, 223, 690
 McLure R. J., Kukula M. J., Dunlop J. S., Baum S. A., O'Dea C. P., Hughes D. H., 1999, *MNRAS*, 308, 377
 Mandelbaum R. et al., 2008, *MNRAS*, 386, 781
 Martini P., Weinberg D. H., 2001, *ApJ*, 547, 12
 Mountrichas G., Shanks T., Croom S. M., Sawangwit U., Schneider D. P., Myers A. D., Pimblet K., 2009, *MNRAS*, 394, 2050
 Myers A. D., Brunner R. J., Nichol R. C., Richards G. T., Schneider D. P., Bahcall N. A., 2007a, *ApJ*, 658, 85
 Myers A. D., Brunner R. J., Nichol R. C., Richards G. T., Schneider D. P., Bahcall N. A., 2007a, *ApJ*, 658, 99
 Nandra K. et al., 2007, *ApJ*, 660, L11
 Navarro J., Frenk C., White S. D. M., 1996, *ApJ*, 462, 563
 Padmanabhan N. et al., 2005, *MNRAS*, 359, 237
 Padmanabhan N. et al., 2007, *MNRAS*, 378, 852
 Padmanabhan N., White M., Eisenstein D. J., 2007, *MNRAS*, 376, 1702
 Porciani C., Norberg P., 2006, *MNRAS*, 371, 1824
 Porciani C., Magliocchetti M., Norberg P., 2004, *MNRAS*, 355, 1010
 Richards G. T. et al., 2002, *AJ*, 123, 2945
 Richards G. et al., 2005, *MNRAS*, 360, 839
 Richards G. et al., 2006, *AJ*, 131, 2766
 Salpeter E. E., 1964, *ApJ*, 140, 796
 Sánchez S. F. et al., 2004, *ApJ*, 614, 586
 Schneider D. P. et al., 2007, *AJ*, 134, 102
 Seljak U., Zaldarriaga M., 1996, *ApJ*, 469, 437
 Seljak U., Sugiyama N., White M., Zaldarriaga M., 2003, *Phys. Rev. D*, 68, 83507
 Serber W., Bahcall N., Menard B., Richards G., 2006, *ApJ*, 643, 68
 Shen Y. et al., 2007, *AJ*, 133, 2222
 Sheth R. K., Tormen G., 1999, *MNRAS*, 308, 119
 Sheth R. K., Mo H. J., Tormen G., 2001, *MNRAS*, 323, 1
 Silverman J. D. et al., 2008, *ApJ*, 679, 118
 Smith R. E. et al., 2003, *MNRAS*, 341, 1311
 Springel V. et al., 2005, *Nat*, 435, 629
 Strand N. E., Brunner R. J., Myers A. D., 2008, *ApJ*, 688, 180
 Tremaine S. et al., 2002, *MNRAS*, 574, 740
 White M., 2002, *ApJS*, 579, 16
 White M., Scott D., 1995, *ApJ*, 459, 415
 White M., Zheng Z., Brown M. J. I., Dey A., Jannuzi B. T., 2007, *ApJ*, 655, L69
 White M., Martini P., Cohn J. D., 2008, *MNRAS*, 390, 1179
 York D. G. et al., 2000, *AJ*, 120, 1579
 Zehavi I. et al., 2005, *ApJ*, 630, 1
 Zheng Z., Coil A. L., Zehavi I., 2007, *ApJ*, 667, 760

APPENDIX A: HALO MODEL

In order to understand the manner in which LRGs and quasars inhabit dark matter haloes, we make use of the halo model (for a review see e.g. Cooray & Sheth 2002). Within this formalism, an accurate prediction of galaxy clustering requires a knowledge of

the occupation distribution of objects in haloes (the HOD) and their spatial distribution. In combination with ingredients from N -body simulations, a specified HOD makes strong predictions about a wide array of galaxy clustering statistics.

Our modelling of galaxy clustering is based on mock catalogues constructed within the HOD framework by populating haloes in a cosmological N -body simulation. We use a high-resolution simulation of a Λ CDM cosmology ($\Omega_M = 0.25 = 1 - \Omega_\Lambda$, $\Omega_B = 0.043$, $h = 0.72$, $n_s = 0.97$ and $\sigma_8 = 0.8$). The linear theory power spectrum was computed by evolution of the coupled Einstein, fluid and Boltzmann equations using the code described in White & Scott (1995). This code agrees well with CMBFAST (Seljak & Zaldarriaga 1996), see e.g. Seljak et al. (2003). The simulation employed 1024^3 particles of mass $8 \times 10^9 h^{-1} M_\odot$ in a periodic cube of side $500 h^{-1}$ Mpc using a TREEPM code (White 2002; for a comparison with other N -body codes see Heitmann et al. 2008). The Plummer equivalent softening was $18 h^{-1}$ kpc (comoving). To check for finite volume and force resolution effects, we also looked at simulations of the same cosmology, with the same number of particles, in boxes $250 h^{-1}$ Mpc and $1 h^{-1}$ Gpc. The $250 h^{-1}$ Mpc box turned out to be too small to model LRG clustering.

For each output, we generate a catalogue of haloes using the Friends-of-Friends (FOF) algorithm (Davis et al. 1985) with a linking length of 0.168 times the mean interparticle spacing. This procedure partitions the particles into equivalence classes by linking together all particles separated by less than a distance b , with a density of roughly $\rho > 3/(2\pi b^3) \simeq 100$ times the background density. A comparison of the mass functions in the $500 h^{-1}$ Mpc and $1 h^{-1}$ Gpc boxes suggests that at low particle numbers FoF tends to overcount the number of haloes. To make the mass functions match in the overlap region, we adjusted the mass of the haloes downward by a factor of $1 - n_{\text{part}}^{-0.8}$ (for a similar correction see Lukic et al. 2007).

To make mock catalogues, we use a halo model which distinguishes between central and satellite galaxies. We choose a mean occupancy of haloes: $N(M) \equiv \langle N_{\text{gal}}(M_{\text{halo}}) \rangle$. Each halo either hosts a central galaxy or does not, while the number of satellites is Poisson distributed about a mean N_{sat} . For each sample, we parametrize $N(M) = N_{\text{cen}} + N_{\text{sat}}$ with five parameters:

$$N_{\text{cen}}(M) = \frac{1}{2} \text{erfc} \left[\frac{\ln(M_{\text{cut}}/M)}{\sqrt{2}\sigma} \right] \quad (\text{A1})$$

and

$$N_{\text{sat}}(M) = \left(\frac{M - \kappa M_{\text{cut}}}{M_1} \right)^\alpha \quad (\text{A2})$$

for $M > \kappa M_{\text{cut}}$ and zero otherwise. Different functional forms have been proposed in the literature, but the current form is flexible enough for our purposes.

Table A1. The HOD parameters from our best-fitting model and used to make the mock LRG catalogues. The meaning of the parameters is given in the text. The χ^2 are for 25 data points.

Slice	M_{cut}	M_1	σ	κ	α	χ^2
1	13.15	13.71	1.16	1.59	0.81	37.62
2	13.20	14.00	1.10	0.37	1.07	26.75
3	13.06	14.03	0.13	1.19	1.38	32.80
4	12.95	14.05	0.17	0.64	1.13	33.25
5	12.98	13.86	0.85	1.53	0.96	41.45
6	13.21	13.90	1.26	1.18	1.33	62.41

Central galaxies always live at the minimum of the halo potential while satellite galaxies are randomly placed assuming an NFW profile (Navarro et al. 1996). If we instead use randomly chosen dark matter particles within haloes, which preserves the anisotropy of the haloes and any substructure, $\xi(r)$ is altered at the 10 per cent level on Mpc scales. The differences on large scales are very small. The concentration of the halo is taken from the N -body simulation, but multiplied by a free (mass-independent) factor to allow galaxies to be more or less concentrated than the dark matter. This detail only affects the predictions on small scales.

Given the 3D galaxy positions, the correlation function is computed out to $10 h^{-1}$ Mpc by direct pair counts, and then extrapolated assuming constant bias and a (dimensionless) mass power spectrum given by the Q model:

$$\Delta_m^2(k) = \Delta_{\text{lin}}^2(k) \frac{1 + Qk^2}{1 + Ak} \quad (\text{A3})$$

with $Q = 10 [2/(1+z)]^{0.75}$ and $A = 1.7 h^{-1}$ Mpc. This form provides a reasonable fit to the DM power spectrum in the simulation over the redshift range of interest. The correlation function is then integrated, making the Limber approximation, to find $\omega(\theta_s)$.

Comparison of different parametrizations for N_{cen} and N_{sat} , different methods for making mock catalogues, different techniques for computing $\omega(\theta_s)$, different ranges and subsets of the data and the different simulations of the same cosmology, indicates that our results for the large-scale bias have systematic uncertainties at the several percent level. In the $500 h^{-1}$ Mpc box, different realizations of the same HOD cause 2 per cent changes in the inferred large-scale bias, because of fluctuations in the galaxy-weighted mean halo mass from Poisson fluctuations in N_{sat} . There is a negligible difference in the $1 h^{-1}$ Gpc box. By running a sequence of boxes of increasing resolution, but with the same large-scale phases, we find that the cumulative mass function changes by 5–10 per cent in the mass range of interest due to structural changes in the simulated haloes with increasing force resolution. We might expect a similar change if we included baryonic cooling and star formation in our simulations. This affects the inferred number density for a given set of HOD parameters. However, the positions, and hence clustering properties, of the haloes are largely unaffected by increasing force resolution. In contrast, the bias of a given halo population is sensitive to finite box size effects on scales a few percent of the box size, and the sensitivity is larger the more biased the halo population under consideration. We choose to measure $\xi(r)$ in the $500 h^{-1}$ Mpc box only out to $10 h^{-1}$ Mpc, because we find systematic differences in halo clustering between the large and small boxes for the rarer haloes. This can be traced to the particular modes chosen in the initial conditions. If we restrict to $10 h^{-1}$ Mpc, the large-scale bias agrees between the two simulations to 2 per cent, less than the random error from the fits. The average halo parameters also agree to within the chain-inferred dispersion. Unfortunately, the halo bias is still slightly scale dependent at $10 h^{-1}$ Mpc, as determined from our $1 h^{-1}$ Gpc simulation, so our results extrapolated assuming constant bias tend to overestimate b by 5–10 per cent. We correct for this overestimate for the values quoted in Table 2.

An investigation of all of these effects leads us to assign a 5 per cent systematic error bar to the large-scale LRG bias estimates we derive. This uncertainty, while comparable to or larger than the statistical error for the LRG sample, is irrelevant for our main conclusions. However, future work on modelling LRGs for galaxy formation and evolution will be limited by theoretical uncertainties, and not observational errors. For making mock catalogues,

including QSOs, we use the $500 h^{-1}$ Mpc box. This allows us to probe further down the mass function. The theoretical inaccuracies, of concern for the LRGs, are much smaller than the observational errors on the QSO–LRG cross-correlations. As shown in Fig. 4, the mock catalogues produced in the $500 h^{-1}$ Mpc box provide a very reasonable description of the LRG clustering on large and small scales.

APPENDIX B: COUNTS OF NEIGHBOURS

Previous authors (Serber et al. 2006; Strand et al. 2008) estimated the clustering of quasars by measuring the overdensities of photometric galaxies around quasars in cylindrical apertures. While these measurements can be related to the correlation functions presented in this paper, there are a number of subtleties in their interpretation that have resulted in confusion in the literature. This appendix attempts to clarify these measurements, as well as compare them with our results.

Following Serber et al. (2006), we define $N_{q,g,r}(R)$ as the average number of photometric galaxies within cylindrical apertures of transverse physical (as opposed to angular) radii R , centred on quasars (q), spectroscopic galaxies (g) and random points (r). If we assume that the photometric sample has a normalized redshift distribution $f(\chi)$, we use the formalism of Section 3, to write

$$N_r(R) = n_r \bar{n}_p \int_0^R 2\pi R' dR' \quad (\text{B1})$$

and

$$N_{q,g}(R) = n_{q,g} \bar{n}_p \int_0^R 2\pi R' dR' \quad (\text{B2})$$

$$\times [1 + \langle f(\chi) \rangle_{q,g} w_{qp}(R')] , \quad (\text{B3})$$

where $n_{r,q,g}$ is the number of random points, quasars and spectroscopic galaxies, \bar{n}_p is the areal density of the photometric sample and w is the projected cross-correlation between the different samples. As in Section 3, $\langle f(\chi) \rangle$ implies the redshift distribution of the photometric sample averaged over the redshift distribution of the spectroscopic sample. Normalizing the random galaxies to the number of spectroscopic targets, we then obtain

$$\frac{N_q}{N_r} = 1 + \frac{\langle f(\chi) \rangle_q}{\pi R^2} \int_0^R 2\pi R' dR' w_{qp}(R') \quad (\text{B4})$$

for the quasars with a similar expression for galaxies. We therefore see that the overdensities measured in Serber et al. (2006) and Strand et al. (2008) can be related to the area-averaged projected correlation function weighted by the redshift distribution of the photometric galaxies at the redshifts of the spectroscopic targets. This implies that the overdensities of the quasars and galaxies cannot be directly compared since they are scaled by *different* weights. Furthermore, the overall amplitude of the overdensities cannot be interpreted without the knowledge of the redshift distribution of the photometric galaxies (which is non-trivial for high-redshift quasars since one is starting to probe the high-redshift tail of the photometric galaxies).

Equation (B4) has the property that it asymptotes to 1 on large scales irrespective of galaxy type. We estimate the scale at which $N_{q,g}/N_r \sim 1$ as follows – the redshift distribution of the photometric galaxies spans approximately $1 h^{-1}$ Gpc and the integral of f must equal unity, suggesting $\langle f(\chi) \rangle \sim 10^{-3} h \text{ Mpc}^{-1}$. Assuming that the cross-correlation between quasars (spectroscopic galaxies) and photometric galaxies is similar to the quasar–LRG cross-correlation,

this implies that the second term of equation (B4) is $\mathcal{O}(1)$ on scales $R \sim 0.1 h^{-1}$ Mpc. Note that this implies that the overdensities are $\mathcal{O}(1)$ on all scales, especially on scales larger than a Mpc. We emphasize that this is simply due to the division by the mean density and in no way implies that the quasars and spectroscopic galaxies have the same large-scale bias or inhabit haloes of similar masses. Note that this is a significant difference between spectroscopic and photometric samples – for spectroscopic samples, the width of the redshift distribution is typically a few tens of Mpc (to integrate out redshift space distortions), and the second term in equation (B4) is much larger than the first. In this case, the overdensities can be directly interpreted as the angle-averaged correlation function. For photometric samples, the complications can be simply circumvented by subtracting 1 from the overdensities, if the redshift distribution of the photometric sample is known (see the discussion above). However, neither Serber et al. (2006) nor Strand et al. (2008) do this when comparing with the galaxy samples, and their results must not be interpreted as quasars having the same clustering. An important corollary to this is that the upturn seen in overdensities cannot be interpreted (as has often been in the literature) as an excess in small-scale clustering, but is simply the signature of a clustered sample of objects. Indeed, as we show below, the cross-correlation for the quasars is consistent with being a power law down to small scales.

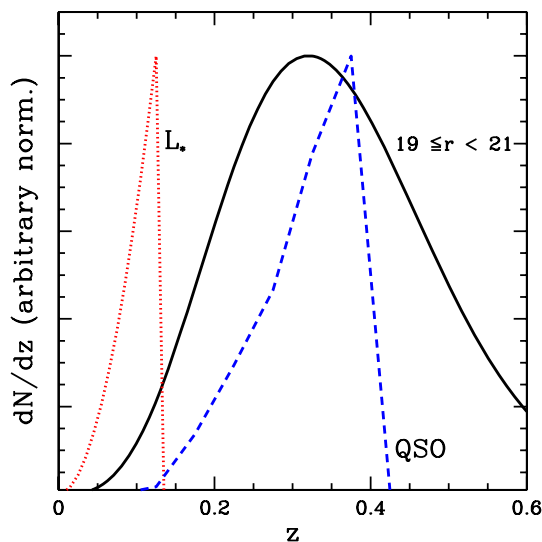


Figure B1. The redshift distributions of spectroscopic L_* galaxies (dotted, red line), photometric galaxies $19 \leq r < 21$ (solid, black line) (Mandelbaum et al. 2008) and spectroscopic quasars with $z \leq 0.4$ (dashed, blue line). Note that the normalizations of the redshift distributions are arbitrary. The figure emphasizes the fact that L_* galaxies and quasars probe very different regions of the photometric redshift distribution, complicating the comparison between their clustering.

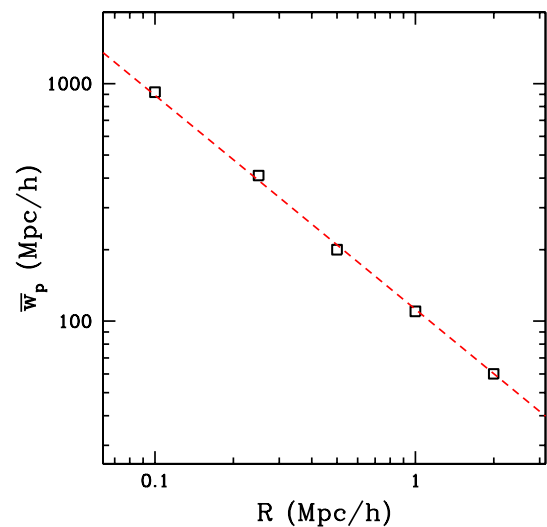


Figure B2. The integrated, projected cross-correlation function, $\bar{w}_{qp}(< R)$, of photometric galaxies and quasars in SDSS from Strand et al. (2008) assuming $f(\chi_q) \approx 10^{-3} h \text{ Mpc}^{-1}$ (see the text). The quoted errors are the size of the plotted symbols. The line is derived from a power-law correlation function with slope 1.9 and $r_0 = 5 h^{-1}$ Mpc.

The final complication in interpreting these results arises due to the width of redshift distribution of the photometric sample. Since the photometric sample covers a large redshift range, it cannot be treated as a homogeneous sample and we cannot model its autocorrelation as we did with the LRGs. In order to interpret the cross-correlation of the quasars with the photometric sample, we must therefore compare it with the cross-correlation between a particular population of galaxies and the photometric sample. Unfortunately, for the SDSS, quasars and galaxies occupy different redshift ranges (see Fig. B1) and therefore probe different subpopulations of the photometric sample. Any comparison between quasars and galaxies must also take into account these population differences, complicating any analysis.

A detailed modelling of all these effects goes well beyond the scope of this appendix. However, as an illustration, we take the results of Strand et al. (2008), subtract 1 and divide by $\langle f(\chi) \rangle \sim 10^{-3} h \text{ Mpc}^{-1}$; the results are in Fig. B2. The clustering is consistent with a 3D power law of slope 1.9 and $r_0 \sim 5 h^{-1}$ Mpc. We remind the reader that the value of r_0 is completely degenerate with our assumption for $\langle f(\chi) \rangle$.

This paper has been typeset from a \LaTeX file prepared by the author.